Electronic Supplementary Material (ESI) for Environmental Science: Nano.

Supporting Information

Efficient removal of low-concentration organoarsenic by Zr-based metal-organic frameworks: Cooperation of defects and hydrogen bonds

Yunyun Xu[a], Jiaxin Lv[a], Yao Song[a], Xiaoyu Zhou[b], Chen Tian[a,*], Xujia Hong[c], Yuepeng Cai[c], Cunyuan Zhao[b], Zhang Lin[a,*]

[a] School of Environment and Energy, The Key Laboratory of Pollution Control and Ecosystem Restoration in Industry Clusters (Ministry of Education), South China University of Technology, Guangzhou, Guangdong 510006, China

[b] MOE Key Laboratory of Bioinorganic and Synthetic Chemistry, School of Chemistry, Sun Yat-Sen University, Guangzhou 510275, P. R. China.

[c] School of Chemistry and Environment, South China Normal University, Guangzhou 510006, China

***Corresponding author:** Zhang Lin, Chen Tian

Tel.: +86-20-39380503

E-mail: zlin@scut.edu.cn (Pro. Zhang Lin), estianchen@scut.edu.cn (Dr. Chen Tian)

Content

S1. Supplemental Materials and Experiments

S2. Supplemental Results and Discussions

23 pages, 8 figures, 7 tables, and 4 equations

S1. Supplemental Materials and Experiments

Analyses of the adsorption data

Nonlinear Langmuir (eq 1) and Freundlich models (eq 2) were employed to fit the isotherms on *p*-ASA and ROX adsorption by UiO-66, UiO-66-D and UiO-66-D-NH_2 after adsorption for 12 h. The adsorption isotherms fitted with the following equations:

$$\frac{C_e}{q_e} = \frac{C_e}{Q_m} + \frac{1}{Q_m K_L} \quad (1)$$

where:

C_e: equilibrium concentration of adsorbate (mg L^{-1});

q_e: amount adsorbed at equilibrium (mg g^{-1});

Q_m: maximum adsorption capacity (mg g^{-1});

K_L: Langmuir affinity coefficient (L mg^{-1})

$$q_e = K_f C_e^{\,n} \quad (2)$$

where :

C_e: equilibrium concentration of adsorbate (mg L^{-1});

q_e: amount adsorbed at equilibrium (mg g^{-1});

K_f: Freundlich affinity coefficient (mg g^{-1});

n: Freundlich exponential coefficient.

The kinetics of *p*-ASA and ROX adsorption was interpreted using a pseudo-second-order nonlinear kinetic model expressed by the following equation:

$$\frac{t}{q_t} = \frac{1}{k_2 q_e^2} + \frac{t}{q_e} \tag{3}$$

where,

q_e: amount adsorbed at equilibrium (mg g^{-1});

q_t: amount adsorbed at time t (mg g^{-1});

t: adsorption time (min);

k_2: the pseudo-second-order rate constant (g mg^{-1} min^{-1}).

Characterization

X-ray diffraction (XRD) data were collected with a D8-Advance X-ray diffractometer (Bruker, German) which had a high-intensity monochromatic nickel-filtered Cu Kα radiation. The 2θ range was from 5 to 80°, and the scan step size was 0.02°.

Field emission scanning electron microscope (FESEM, Nova, Nano SEM 430, FEI Company) was operated at an acceleration voltage of 15 kV.

Brunauer-Emmett-Teller (BET) specific surface area (SSA) of the samples were determined by collecting N_2 gas adsorption/desorption isotherms, which was on a Micromeritics ASAP 2020 Instrument. Before the SSA determination, all samples of MOFs were degassed at 200 °C for 18 h. The specific surface areas for N_2 were calculated under the N_2 pressure($0.005 < P/P_0 < 0.1$). The pore size distributions were calculated from the adsorption-desorption isotherms *via* density functional theory (DFT) and Barrett-Joyner-Halenda (BJH) model.

Thermogravimetric analysis (TGA) experiments data were collected using STA

449C simultaneous thermal analyzer (NETZSCH, Germany). With a heating rate of 5 ºC min^{-1}, 20 mg samples were heated from 25 to 600 ºC under a 30% O_2/N_2 (3:7, V/V) gas flow (90 mL min^{-1}). The TG-MS was conducted under argon atmosphere and the heating rate was 5 ºC min^{-1}.

Fourier transform infrared spectroscopy (FTIR) data were collected *via* KBr discs on a Vector 33 spectrometer (Bruker, Germany). The FTIR spectra were recorded over a spectral window, and the range was from 400 to 4000 cm^{-1}.

X-ray photoelectron spectroscopy (XPS) spectra were analyzed *via* an Axis Ultra DLD instrument (Kratos Analytical, U.K.) with an A1 Kα X-ray source. Spectra were recorded at a pass energy (160 eV) for survey scans and for high-resolution scans (40 eV).

Extended X-ray absorption fine structure (EXAFS) data collection and analysis

The *K*-edge EXAFS spectra of As in *p*-ASA (or ROX)-loaded samples at room-temperature measurements were collected in the beamline 4W1B of the Beijing Synchrotron Radiation Facility (BSRF). A Lytle detector, which was equipped with Soller slits and Ge filter, was used for screening scattering and fluorescence background. At 11875 eV, the maximum absorption edge As was set. The EXAFS data was performed by ATHENA and ARTEMIS interfaces to the IFEFFIT version 1.2.11 program package.

DFT calculations

DFT calculations were performed using the Vienna ab initio simulation package (VASP), including the Perdew-Burke-Ernzerhof (PBE) functional and the potential projector augmented wave (PAW) pseudo-potentials. The plane-wave cut off energy was set to 500 eV. The scalar relativistic effect was introduced into the effective core potentials by explicit mass-velocity and Darwinian correction. The conjugate-gradient algorithm was used for the ion relaxation, which was based on Hellmann-Feynman forces. Geometry optimizations were performed, and the total energy converged to under 1×10^{-4} eV with forces on all atoms which were less than 0.02 eV $Å^{-1}$. After using the Poisson-Boltzmann implicit solvation model with a dielectric constant for water ($\varepsilon = 78.4$), Solvation corrections were calculated for each system. Besides, the long-range dispersion corrections, also named as van der Waals interactions, were evaluated *via* DFT-D3 (BJ) method.

The binding energy (Eb) of *p*-ASA with UiO-66 was calculated by the following equation:

$$\text{Eads} = \text{Esc} - \text{E'sc} \tag{4}$$

Where:

Esc: the energy of the optimized binding complex;

E'sc: the corresponds to the energy of a system for which the *p*-ASA and UiO-66 are kept apart.

S2. Supplemental Results and Discussions

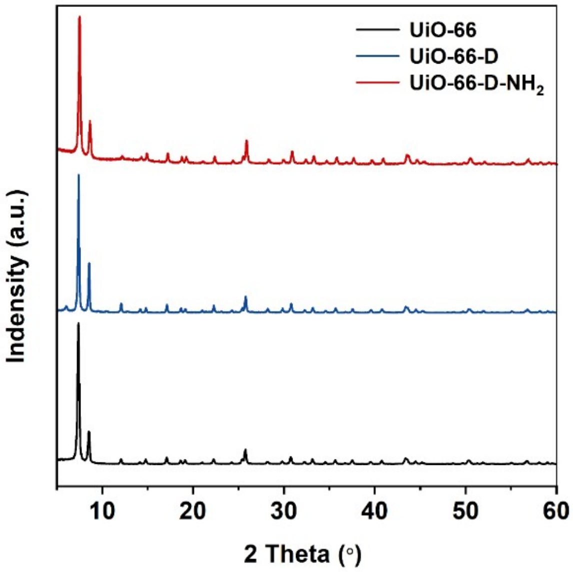

Fig. S1. XRD patterns of UiO-66 MOFs.

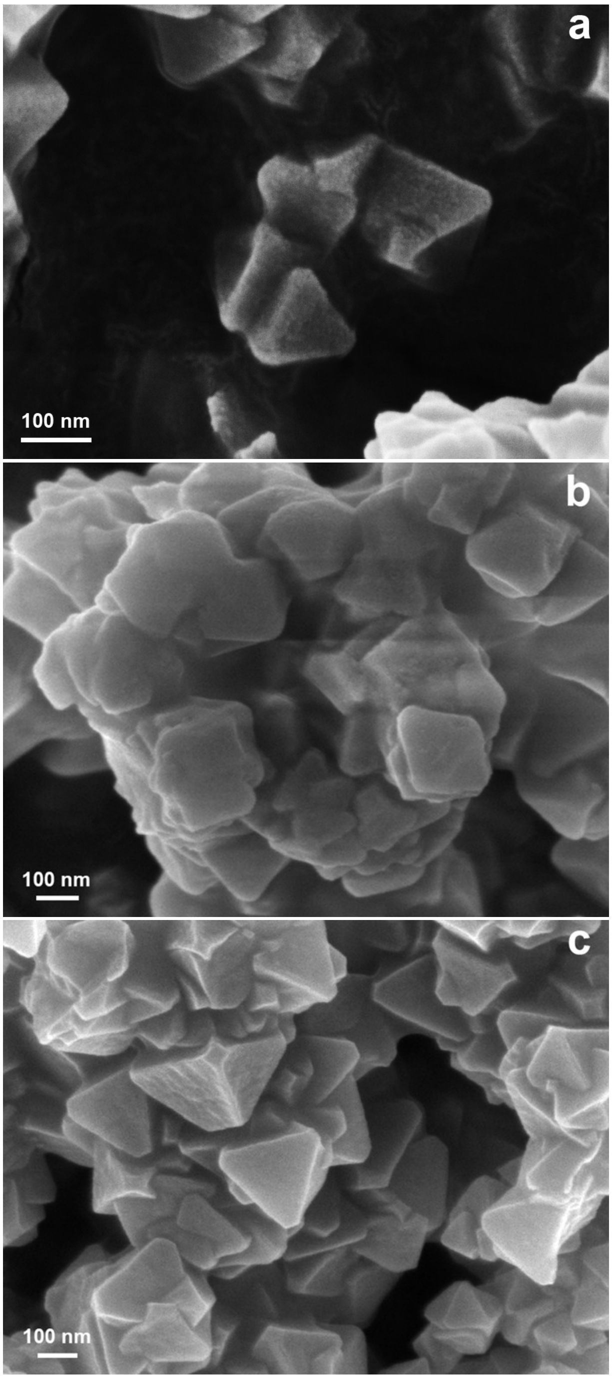

Fig. S2. SEM of (a) UiO-66, (b) UiO-66-D and (c) UiO-66-D-NH_2.

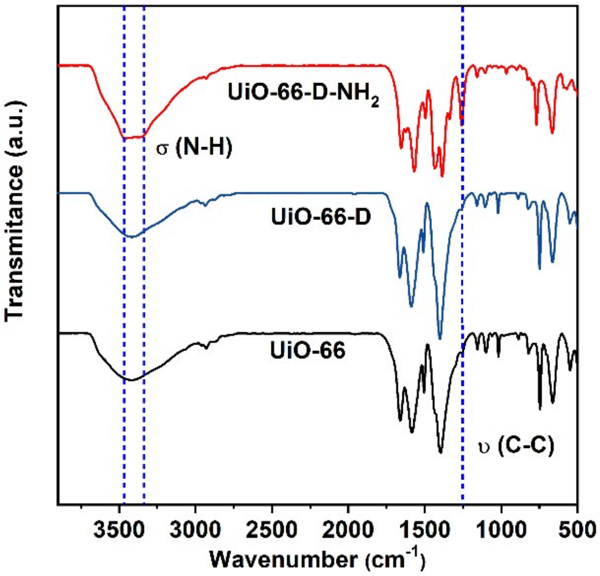

Fig. S3. FTIR spectra of UiO-66 MOFs.

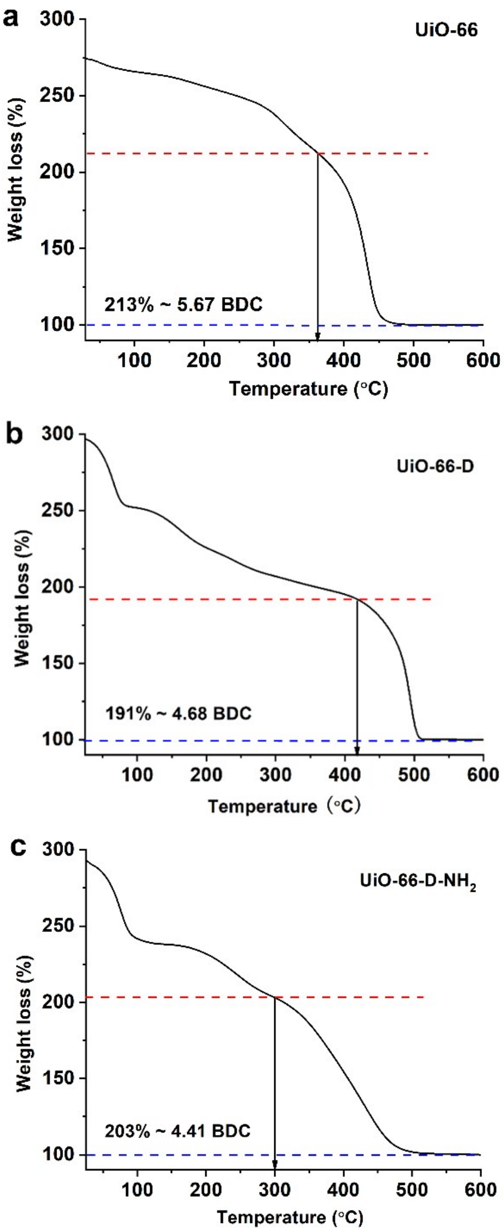

Fig. S4. TGA curves of (a) UiO-66, (b) UiO-66-D and (c) UiO-66-D-NH_2. The mass residues at 500 °C is presumably belonged to ZrO_2. The mass loss due to the organic linkers is calculated from the mass at ~ 360 °C for UiO-66, ~ 420 °C for UiO-66-D and ~ 300 °C for UiO-66-D-NH_2 to the point of complete linker degradation. The calculation of actual number of linkers in each adsorbent please see in Table S3.

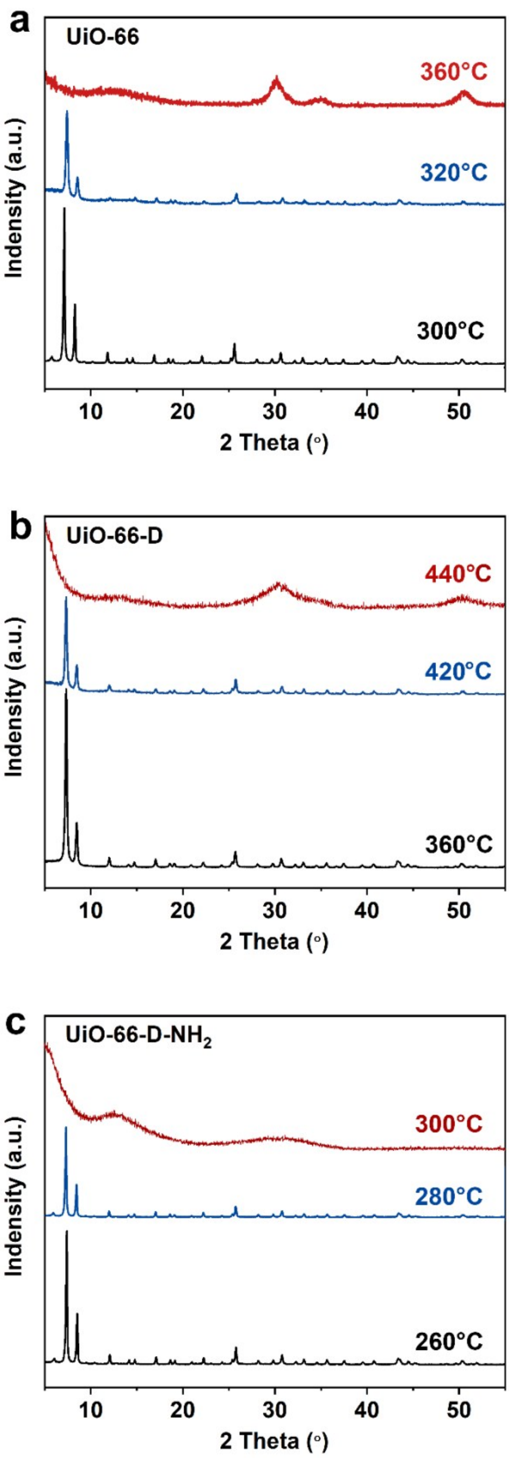

Fig. S5. Temperature-dependent XRD patterns of (a) UiO-66, (b) UiO-66-D and (c) UiO-66-D-NH$_2$. The temperature at which the crystal structure collapses is consistent with the decomposition temperature in TGA curves (Fig S4).

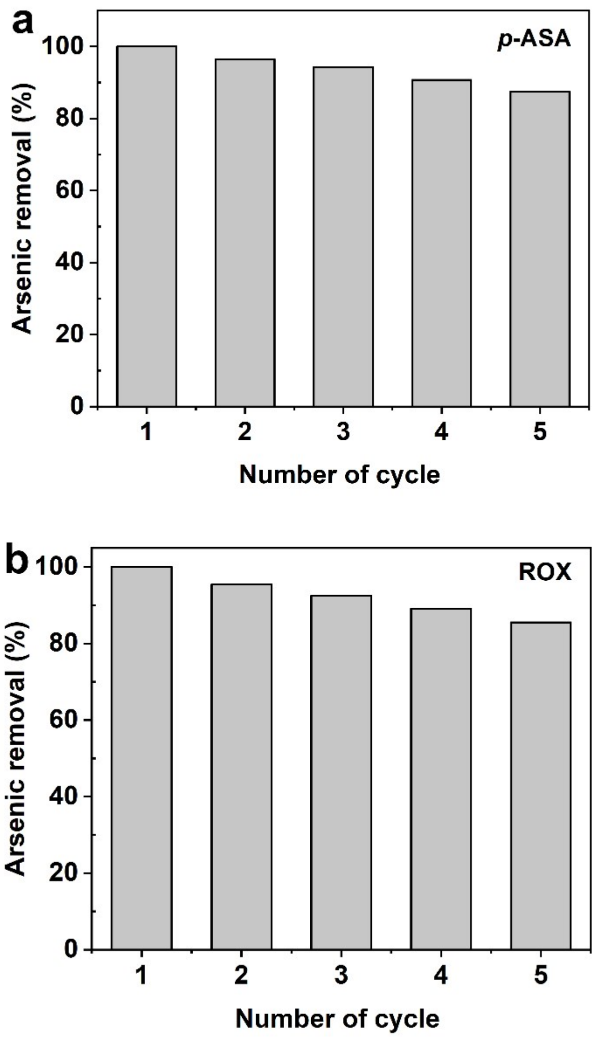

Fig. S6. Regeneration of UiO-66-D-NH_2 in (a) *p*-ASA and (b) ROX. The initial concentration of *p*-ASA and ROX was 50 mg L^{-1} for all the treatments. The desorption agent was 0.5 mol L^{-1} NaOH/ethanol solution.

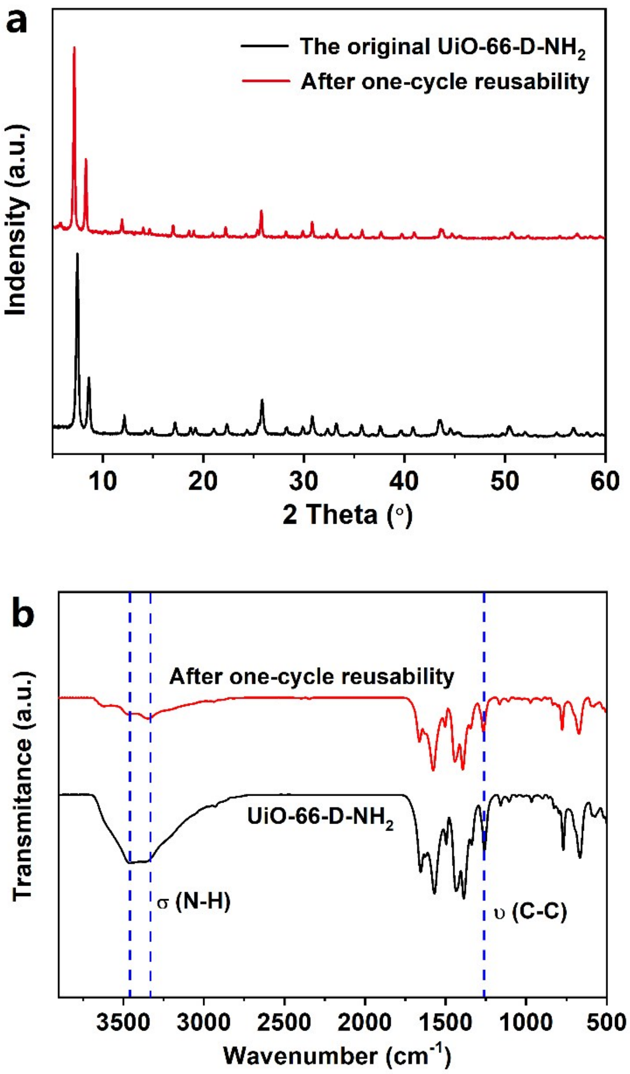

Fig. S7. (a) XRD pattern and (b) FTIR spectra of UiO-66-D-NH_2 before and after regeneration.

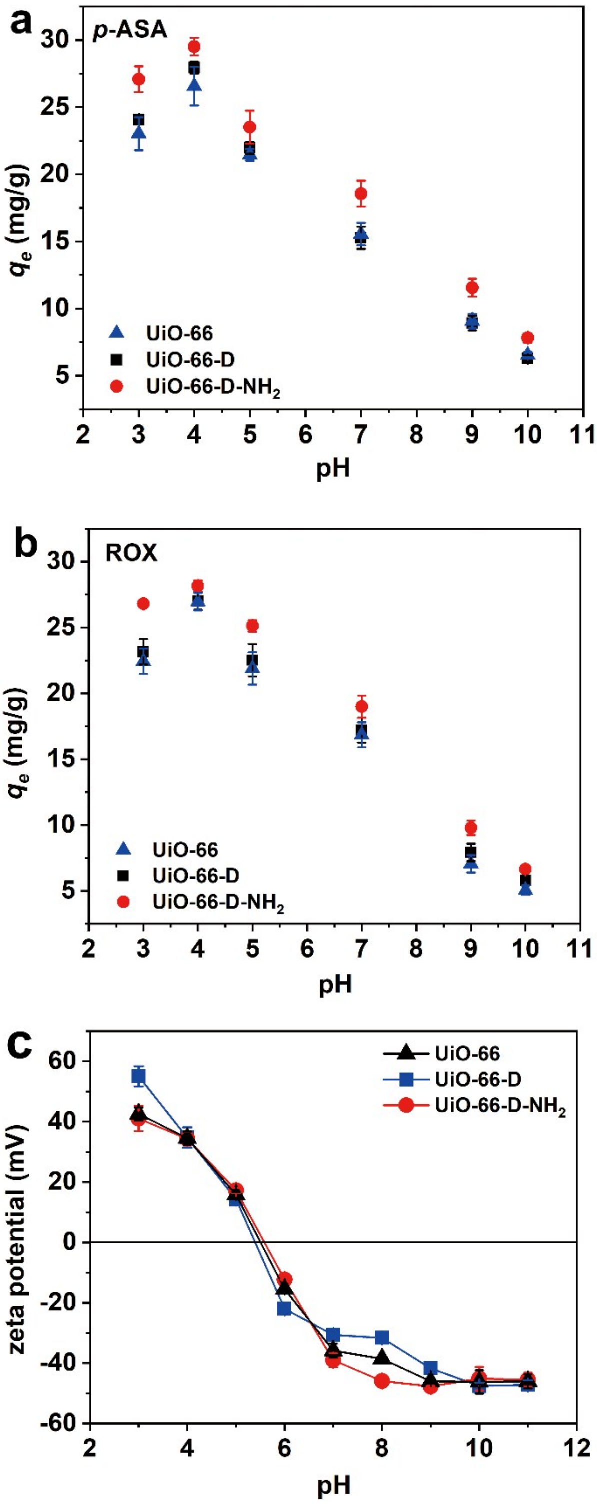

Fig. S8. (a) *p*-ASA and (b) ROX uptake by UiO-66, UiO-66-D and UiO-66-D-NH$_2$ as a function of solution pHs, (c) Zeta potentials of UiO-66, UiO-66-D and UiO-66-D-NH$_2$ as a function of solution pHs.

Table S1. The element content in UiO-66-D-NH_2 of XPS analysis.

Element	Atomic mass %
C	57.98
N	6.38
Zr	4.39
O	31.25

The mole ratio of -NH_2: Zr per node was calculated from the atomic ratio of N: Zr obtained from the XPS data and -NH_2: Zr = 1.45, thus each BDC-NH_2 linker in UiO-66-D-NH_2 contained two -NH_2 in theory.

Table S2. BET analyses of surface area and pore size of UiO-66 MOFs.

Material	BET surface area (m^2 g^{-1})	Pore Size (Å)
UiO-66	1134.61	8.96
UiO-66-D	1371.14	9.29
UiO-66-D-NH_2	974.43	5.00

Table S3. The theoretical mass loss as a function of n. The n stands for the ligand number $Zr_6O_6(BDC)_n$ and $Zr_6O_6(BDC\text{-}(NH_2)_2)_n$.

n	Theoretical Mass loss(%)	
	$Zr_6O_6(BDC)_6$	$Zr_6O_6(BDC\text{-}(NH_2)_2)_6$
1	109	113
2	131	140
3	154	166
4	176	192
5	198	218
6	220	245
	Actual Mass loss(%)	
4.7	191	-
4.4	-	203

The mass residual of UiO-66 was close to the theoretical weight. The molecular weight of UiO-66-D and UiO-66-D-NH_2 are 191% and 203% times as high as 6 ZrO_2, meaning that the frameworks were lighter than the idealized equation (220% and 245%). The linker number in each unit of UiO-66-D and UiO-66-D-NH_2 is calculated to be 4.7 and 4.4, respectively. Each Zr-node has 6 linkers in theory, and one linker losing produces two defects. Therefore, the defects in UiO-66-D and UiO-66-D-NH_2 are calculated to be 2.6 and 3.2, respectively.

Table S4. Comparison of Langmuir and Freundlich model parameters for adsorption on various adsorbents.

		Langmuir model			Freundlich model		
	Samples	Q_m (mg g^{-1})	K_L (L mg^{-1})	R^2	$1/n$	K_f (mg g^{-1})	R^2
p-ASA	UiO-66	59.17	1.82	0.999	0.58	35.85	0.959
	UiO-66-D	68.49	3.84	0.995	0.62	69.32	0.987
	UiO-66-D-NH_2	98.04	6.38	0.995	0.75	199.30	0.994
	ZrO_2	24.10	1.65	0.993	0.20	14.89	0.965
ROX	UiO-66	59.17	1.92	0.998	0.57	36.42	0.969
	UiO-66-D	70.42	2.84	0.993	0.64	62.38	0.992
	UiO-66-D-NH_2	90.91	7.33	0.996	0.70	174.85	0.991
	ZrO_2	23.31	1.90	0.998	0.22	14.36	0.971

Table S5. The *p*-ASA and ROX adsorption capacity and affinity of different types of adsorbents obtained from Langmuir-fitting results.

Adsorbents	Pollutant	C_0 (mg L^{-1})	Q_m (mg g^{-1})	K_L (L g^{-1})	${}^aK_{0.01}$ (L g^{-1})	${}^bq_{e0.01}$ (mg g^{-1})	Ref.
UiO-67	*p*-ASA	1-100	484	0.28	126	3.78	[1]
UiO-67-NH_2		1-100	178	0.83	150	4.50	[1]
Mesoporous ZIF-8		3-350	791	0.032	25.4	0.76	[2]
AC		12-200	239	0.063	15.0	0.45	[3]
MIL-100-Fe		12-200	366	-			[3]
Iron humater		20	169	0.038	6.41	0.19	[4]
UiO-66		1-10	59	1.82	107	1.06	This work
UiO-66-D		1-10	68	3.84	236	7.08	This work
UiO-66-D-NH_2		1-10	98	6.38	613	18.4	This work
ZrO_2		1-10	24	1.65	40	1.19	This work
Fe_3O_4@RGO	ROX	1-100	454	0.78	346	10.4	[5]
Porous magnetic carbon composites		50-500	417	0.21	86.3	2.59	[6]
UiO-66 with defects		10-200	730	0.11	80.0	2.40	[7]
Hydrochar-derived magnetic carbon		50-500	588	0.063	37.0	1.11	[8]
Chitosan-based copolymers		1000	259	0.090	23.2	0.70	[9]
Ferric and manganese binary oxide		5-275	142	-			[10]
Multi-walled carbon nanotubes		5-40	13	0.122	1.58	0.047	[11]
UiO-66		1-10	59	1.92	113	1.11	This work
UiO-66-D		1-10	70	2.84	198	5.95	This work
UiO-66-D-NH_2		1-10	91	7.33	652	19.6	This work
ZrO_2		1-10	23	1.90	44	1.32	This work

${}^aK_{0.01}$ is single point adsorption coefficient when $C_{e\text{-}As}$ = 10 μg L^{-1}. The arsenic standard in drinking water of WHO is 10 μg L^{-1}. ${}^bq_{e0.01}$ is the equilibrium adsorption capacity calculated from the Langmuir model when $C_{e\text{-}As}$ = 10 μg L^{-1}.

Table S6. Parameters of pseudo-second order kinetic for adsorption on UiO-66, UiO-66-D and UiO-66-D-NH_2.

	Pseudo-second order kinetic			
	Samples	q_e (mg g^{-1})	k_2 (g mg^{-1} min^{-1})	R^2
p-ASA	UiO-66	26.04	0.051	0.9999
	UiO-66-D	26.39	0.090	0.9999
	UiO-66-D-NH_2	28.65	0.230	0.9999
ROX	UiO-66	24.10	0.045	0.9999
	UiO-66-D	28.09	0.047	0.9999
	UiO-66-D-NH_2	28.25	0.106	0.9999

Table S7. Results of shell-by-shell fitting from EXAFS data of ROX-adsorbed and *p*-ASA-adsorbed samples.

Sample	Atomic path	[a]CN	[b]R (Å)	[c]σ^2 (Å)	[e]*R*-factor
p-ASA: UiO-66	As-O	3.7	1.701(0.03)	0.002	0.020
	[f]As-Zr	0.6	3.492(0.05)	0.006	
	[g]$\text{MS}_{\text{As-O-O}}$	10	2.835(0.02)	0.002	
p-ASA: UiO-66-D	As-O	3.7	1.695(0.04)	0.004	0.021
	[f]As-Zr	0.6	3.463(0.04)	0.004	
	[g]$\text{MS}_{\text{As-O-O}}$	10	2.996(0.03)	0.001	
p-ASA: UiO-66-D-NH$_2$	As-O	3.7	1.695(0.04)	0.002	0.026
	[f]As-Zr	1.8	3.409(0.09)	0.005	
	[g]$\text{MS}_{\text{As-O-O}}$	10	3.051(0.02)	0.002	
ROX: UiO-66	As-O	3.8	1.683(0.04)	0.004	0.023
	[f]As-Zr	0.8	3.547(0.06)	0.007	
	[g]$\text{MS}_{\text{As-O-O}}$	10	2.965(0.03)	0.002	
ROX: UiO-66-D	As-O	3.8	1.694(0.04)	0.004	0.019
	[f]As-Zr	1.1	3.451(0.05)	0.007	
	[g]$\text{MS}_{\text{As-O-O}}$	10	2.987(0.04)	0.001	
ROX: UiO-66-D-NH$_2$	As-O	3.9	1.694(0.04)	0.003	0.026
	[f]As-Zr	1.5	3.433(0.07)	0.009	
	[g]$\text{MS}_{\text{As-O-O}}$	10	2.992(0.03)	0.001	

[a]CN: number of neighbors. [b]R (Å): Interatomic distances. [c]σ^2 (Å): Debye-Waller factor. [d]R-factor:

goodness of fitting. [f]$MS_{As\text{-}O\text{-}O}$: multiple scattering. The amplitude reduction factor ($S0^2$) was fixed of 0.95. Numbers in the parentheses are standard errors of the fitted parameters.

References:

1 Tian, C.; Zhao, J.; Ou, X.; Wan, J.; Cai, Y.; Lin, Z.; Dang, Z.; Xing, B., Enhanced Adsorption of *p*-Arsanilic Acid From Water by AmineModified UiO-67 as Examined Using Extended X-Ray Absorption Fine Structure, X-Ray Photoelectron Spectroscopy, and Density Functional Theory Calculations. *Environ. Sci. Technol.*, 2018, **52**, 3466-3475.

2 Jung, B. K.; Jun, J. W.; Hasan, Z.; Jhung, S. H., Adsorptive Removal of *p*-Arsanilic Acid From Water Using Mesoporous Zeolitic Imidazolate Framework-8. *Chem. Eng. J.*, 2015, **267**, 9-15.

3 Jun, J. W.; Tong, M.; Jung, B. K.; Hasan, Z.; Zhong, C.; Jhung, S. H., Effect of Central Metal Ions of Analogous Metal–Organic Frameworks on Adsorption of Organoarsenic Compounds from Water: Plausible Mechanism of Adsorption and Water Purification. *Chemistry-A European Journal*, 2015, **21**, 347-354.

4 Peng, Y.; Wei, W.; Zhou, H.; Ge, S.; Li, S.; Wang, G.; Zhang, Y., Iron Humate as a Novel Adsorbent for p-Arsanilic Acid Removal from Aqueous Solution. *J. Disper. Sci. Technol.*, 2016, **37**, 1590-1598.

5 Tian, C.; Zhao, J.; Zhang, J.; Chu, S.; Dang, Z.; Lin, Z.; Xing, B., Enhanced Removal of Roxarsone by Fe_3O_4@3D Graphene Nanocomposites: Synergistic Adsorption and Mechanism. *Environmental Science: Nano*, 2017, **4**, 2134-2143.

6 Zhu, X.; Qian, F.; Liu, Y.; Matera, D.; Wu, G.; Zhang, S.; Chen, J., Controllable Synthesis of Magnetic Carbon Composites with High Porosity and Strong Acid Resistance From Hydrochar for Efficient Removal of Organic Pollutants: An

Overlooked Influence. *Carbon*, 2016, **99**, 338-347.

7 Li, B.; Zhu, X.; Hu, K.; Li, Y.; Feng, J.; Shi, J.; Gu, J., Defect Creation in Metal-Organic Frameworks for Rapid and Controllable Decontamination of Roxarsone From Aqueous Solution. *J. Hazard. Mater.*, 2016, **302**, 57-64.

8 Zhu, X.; Qian, F.; Liu, Y.; Zhang, S.; Chen, J., Environmental Performances of Hydrochar-Derived Magnetic Carbon Composite Affected by its Carbonaceous Precursor. *RSC Adv.*, 2015, **5**, 60713-60722.

9 Poon, L.; Younus, S.; Wilson, L. D., Adsorption Study of an Organo-Arsenical with Chitosan-Based Sorbents. *J. Colloid Interf. Sci.*, 2014, **420**, 136-144.

10 Joshi, T. P.; Zhang, G.; Jefferson, W. A.; Perfilev, A. V.; Liu, R.; Liu, H.; Qu, J., Adsorption of Aromatic Organoarsenic Compounds by Ferric and Manganese Binary Oxide and Description of the Associated Mechanism. *Chem. Eng. J.*, 2017, **309**, 577-587.

11 Hu, J.; Tong, Z.; Hu, Z.; Chen, G.; Chen, T., Adsorption of Roxarsone From Aqueous Solution by Multi-Walled Carbon Nanotubes. *J. Colloid Interf. Sci.*, 2012, **377**, 355-361.